energy&fuels

Article

pubs.acs.org/EF

Hydrogen Production from Water Vapor Plasmolysis Using DBD-Corona Hybrid Reactor

Fahad Rehman,* Wameath S. Abdul Majeed, and William B. Zimmerman

Department of Chemical and Biological Engineering, University of Sheffield, Mappin Street Sheffield, S1 3JD, United Kingdom

ABSTRACT: Hydrogen is produced by plasmolysis of (1) demineralized water vapors (steam) and (2) water vapor and argon gas. In the current study, a custom-made dielectric barrier discharge (DBD)-corona hybrid reactor has been designed and used for steam plasmolysis. The objective is to show the feasibility of hydrogen production from water vapor plasmolysis at atmospheric pressure at a relatively smaller interelectrode distance and to characterize the plasma for its fundamental properties. The generated plasma properties have been characterized by applying spectrometric analysis, in which the measured plasma temperatures are demonstrated in the order $T_e > T_{exc} > T_{rot}$, which confirms the nonlocalized thermal equilibrium (LTE) existence in the plasma bulk. Moreover, the estimated electron number density (1.765×10^{17} m^{-3}) shows an exceptional energy for water vapor dissociation, which eventually results in a reasonable efficiency. The estimated energy efficiency and thermodynamic efficiency for water vapor plasmolysis along with steam was found to be 78.8% and 79.2%, respectively. Accordingly, the calculated production rate (20 g/kWh) and the predicted cost (£0.09/kWh) are shown to be competitive to the electrolysis process, which is increasingly applied for hydrogen production, with the benefit of reduced equipment size and low power consumption.

1. INTRODUCTION

Since 1970s embargo, interest in the alternative fuels were developing to power our society.[1] The increasing cost, depletion, and adverse environmental issues of fossil fuel utilization have raised serious concerns in the society about long-term usage and sustainability. To cope with these issues, continuous efforts are made to find cleaner, sustainable fuel at comparable price with fossil fuel.[2] However, alternative fuels are not available everywhere on demand. One possible solution is the utilization of the hydrogen which is known as energy carrier for approximately two centuries now.[3] It can be produced from multiple sources, which include coal and natural gas and renewable sources such as biomass, hydropower, geothermal, solar and wind power.[4] However, problems such as economical production, separation of H_2/O_2 mixture, and storage are the barriers yet to be overcome.

Hydrogen production by plasmolysis of water has been studied by both theoretically and experimentally.[5−11] Fridman[9] has discussed water vapor breakdown by different mechanisms and pointed out chemical reactions responsible for initiation, propagation, and termination of water vapor plasmolysis. Full details of water vapor dissociation by vibrational excitation channel and dissociative attachment of electron channel are given. More recently, Rehman[11] showed detailed discussion of the kinetic modeling of hydrogen formation from water vapor plasmolysis in plasma microreactors. Key kinetic steps governing the breakdown have been identified.

Jasinski[12] and Wang[13] studied steam reforming with plasma in different plasma environments. Other than water, methane and natural gas were studied as feedstock by Mutaf-Yardimci[14] and Boutot,[15] respectively. Plasma electrolysis has also been studied for hydrogen production.[16,17] Different hydrocarbon feedstocks have also been studied[18,19] including methanol,[20] ethanol,[21] and kerosene oil.[22] Steam methane reforming (SMR) and water electrolysis have been considered to be the most straightforward ways to produce hydrogen.[23] Hydrogen production by water vapor plasmolysis using conventional plasma reactors has always been viewed as an expensive route,[24] trailing behind electrolysis and about on par with thermochemical cycles. However, recently, Lozano-Parada and Zimmerman[25] showed a potential for economical production of ozone using microplasma reactor at 170 V AC and 100 Hz. Plasma microreactors produce high electric fields at relatively low voltage, which produces energetic species such as H, OH, and HO_2, etc., at atmospheric pressure. These active species through a series of reactions combine together to eventually form H_2 and O_2.

Typical examples of nonthermal atmospheric pressure plasmas are corona discharges and dielectric barrier discharge (DBD).[26] Corona discharges are considered suitable for various industrial processes as this type of discharges generates a high concentration of radicals. However, continuous corona discharges have a very low power, which is unacceptable for many applications. Voltages could be increased to raise the power level, but this leads to corona transition into arcs. Arcing could be prevented by covering one or both electrodes with dielectric material or by creating corona discharge with pulse-periodic mode.[27] By introducing a dielectric layer, the discharge current is limited, arcing could be avoided between two electrodes, and homogeneous discharge could be created.[18] Therefore, many of DBD-corona hybrid reactors have been designed to overcome these difficulties and take advantage of both high concentration of radicals in corona discharges and homogeneity of plasma discharge at higher power in DBD.[26]

Received: December 3, 2012
Revised: April 14, 2013
Published: April 17, 2013

dx.doi.org/10.1021/ef301981f | *Energy Fuels* 2013, 27, 2748−2761

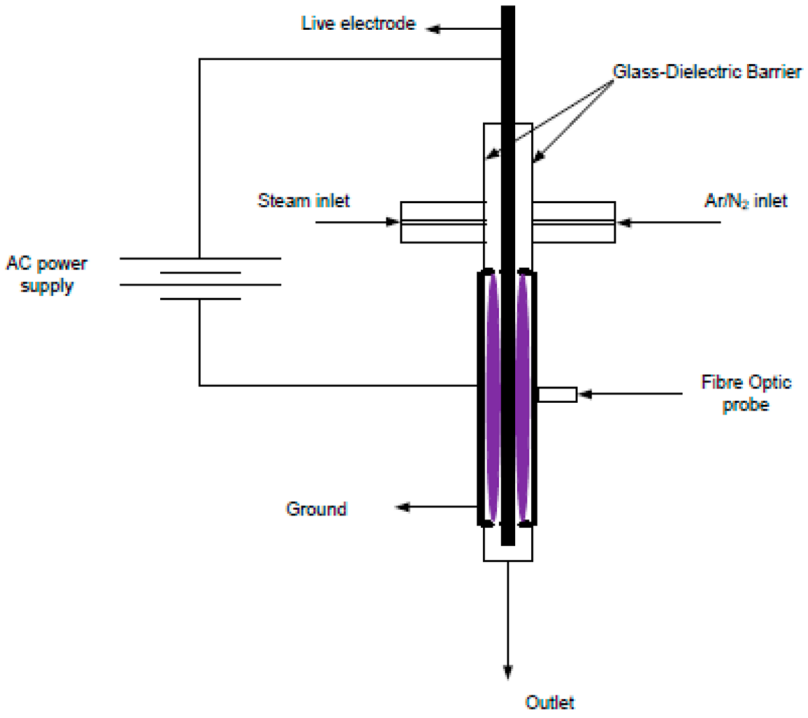

Figure 1. DBD-corona hybrid reactor used in the experiment.

In the current study, a DBD-corona hybrid reactor has been designed and used for steam plasmolysis. The objective is to (1) show feasibility of hydrogen production by water vapor plasmolysis at atmospheric pressure at a relatively smaller interelectrode distance and (2) characterize the plasma for its fundamental properties. The paper is divided into five sections. In the first section, an introduction of the study is given. Section 2 deals with the experimental procedure, followed by section 3, in which a detailed analysis is shown. In section 4, a discussion is presented on the detection of the peaks in the spectral range 317−400 nm. An experiment with underwater plasma is carried out to prevent the contact of plasma discharge with glass surface and simultaneously remove nitrogen from the system. The contact angle of demineralized water with glass slide has been measured after subjecting it to plasma treatment. Finally in section 5, conclusions are given.

2. EXPERIMENTAL SECTION

A custom-made high voltage power source (Entwicklung Leistungselectronic, Germany) was used to ignite the plasma. The power source is designed to give voltage up to 12 kV with frequency ranging from 20 kHz to 40 kHz. The power supply is equipped with manual control knobs to control voltage, current, and frequency. It also has two digital LCDs to monitor voltages and current values. No matching network has been provided in the device due to limited frequency range. A T-shaped borosilicate glass reactor was designed and built with 7 mm outer diameter and 4.88 mm inner diameter. A stainless steel circular rod of diameter 2.40 mm was used as live electrode. Figure 1 shows the schematic representation of reactor. The configuration produced a flow channel 2.48 mm with a radial gap of 1.24 mm. An aluminum sheet of thickness 0.5 mm and 2 cm long has been wrapped around the reactor and used as ground electrode. A 3 mm hole in the center of the ground electrode served as window for data acquisition.

Three different sets of experiments were performed. In the first set of experiments, steam plasma was characterized. In part 1, only water vapors were run through the reactor. Flow rate of water vapor was set to 2 mL/min at 1 atm. Power was supplied from the above-mentioned power source to obtain steam plasma. This was followed by the injection of argon gas at 10 mL/min from the other side of the reactor. Lastly, argon gas was replaced by 10 mL/min of nitrogen into the reactor along with steam. The gases (Ar and N_2) have been injected through an inlet opposite to that used for steam in order to prevent condensation. Both argon and nitrogen were 99.998% pure and bought from BOC.

In the second set of experiments, water vapor decomposition was monitored by connecting a set of condensers to the outlet of the reactor. The experiment was run for ten minutes and steam condensate was collected in a measuring cylinder. The experiment was repeated with injection of argon gas and water vapor decomposition rate was monitored. An empirical model was generated by applying an experimental design plan according to the second order central composite rotatable design[28] to study the effects of steam and argon flow rates on the decomposition rate.

A third set of experiments was carried out to explore the identity of the peaks in 317−400 nm range. Two experiments were carried out separately here. In the first experiment, plasma was ignited in a tube filled with demineralized water between electrodes having interelectrode distance of about 1 mm (Figure 13). In the second experiment, glass chip was treated with argon plasma. The contact angle for demineralized water was measured before and after experiment by First Ten Angstrom tensiometer using the sessile drop method.

The applied voltage was measured by using a high voltage probe and digital oscilloscope (ADC-212, Pico Technology Limited) to generate voltage and frequency output signal. Plasma current was measured by a calibrated digital current clamp meter (UNI-T, UT 201).[29] The experiment was started with an initial voltage of 2.2 kV and gradually increased until 4 kV.

Emission spectra were obtained by a fiber optic sensor, which was collated by (Ocean Optics USB 2000). The spectral data obtained were analyzed by Spectra Suite software (Ocean Optics). This spectrometric system has 0.3−1.5 nm full width half maximum (fwhm) resolution, 600 lines grating density blazed at 300 nm and 25μm slit width. The spectrometric parameters, integration time, and boxcar width were 1000 ms and 2, respectively.[29] All spectral data were recorded at 4 kV, 16 mÅ, and 36.74 kHz.

dx.doi.org/10.1021/ef301981f | *Energy Fuels* 2013, 27, 2748−2761

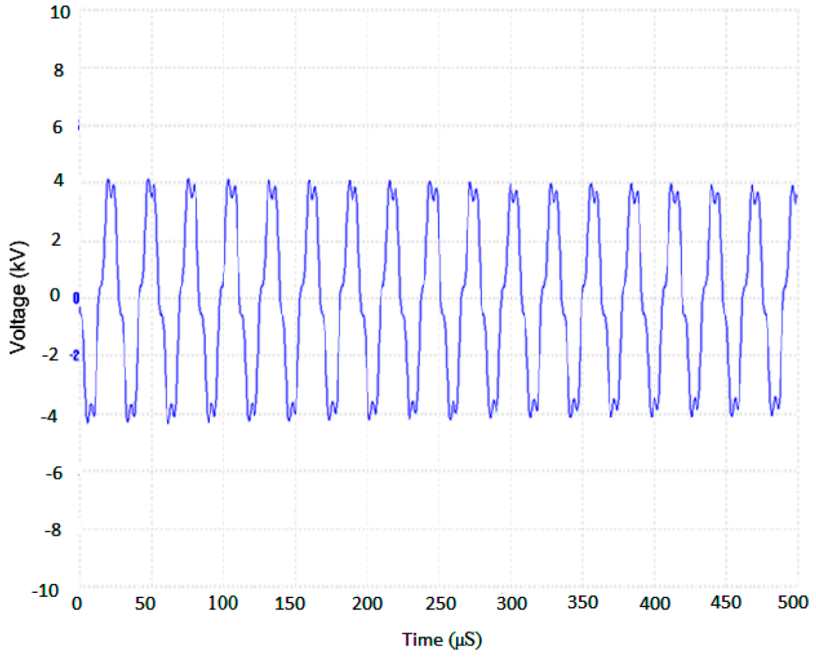

Figure 2. Voltage output signal of the power supply.

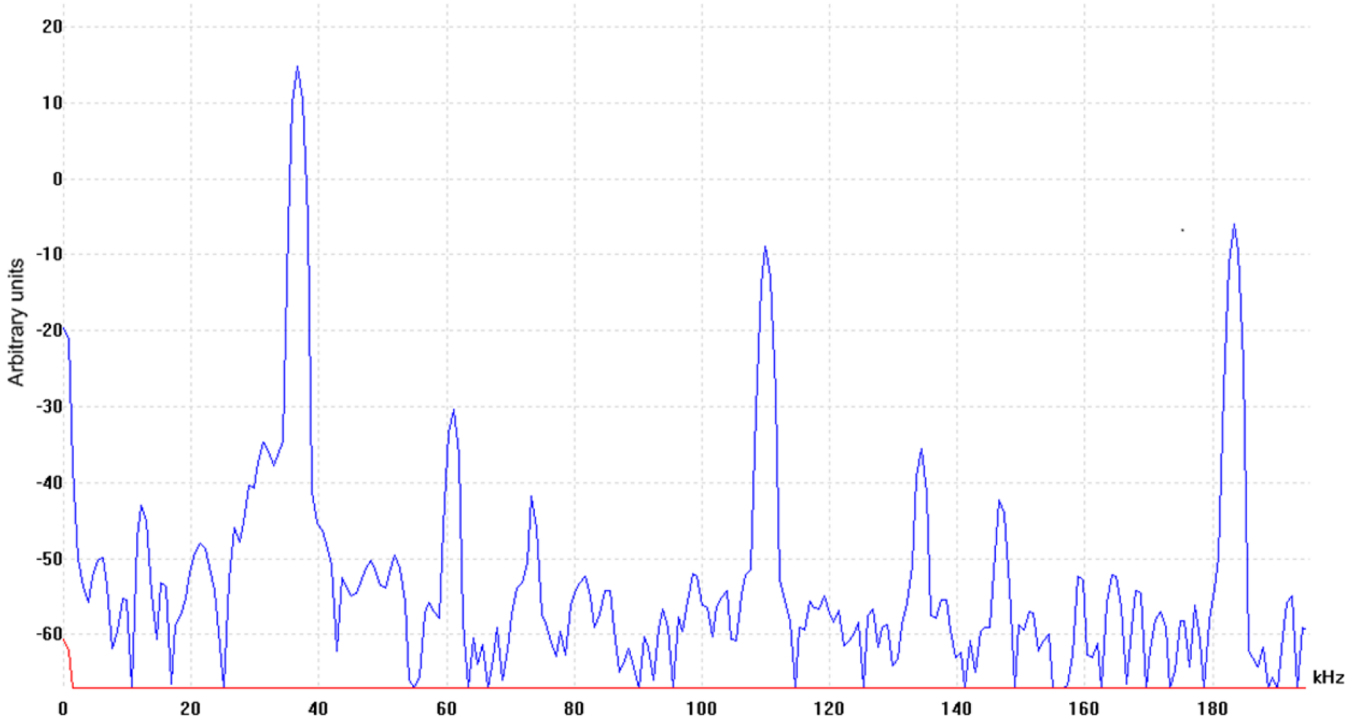

Figure 3. Frequency spectrum showing the output signal mainly at 36.74 kHz.

3. ANALYSIS

3.1. Plasma Characterization. Voltage output signal of the power supply is shown in Figure 2. It is worth monitoring the output signal of the power supply as instabilities may occur in plasma because of the distorted signal. From Figure2, it is evident that the source is providing a stable signal at 4 kV. Figure 3 shows the frequency signal. On the *y*-axis, the amplitude is in arbitrary units. The output signal mainly consisted of one main frequency of 36.74 kHz and two harmonics that are relatively negligible; thus, power goes into the reactor at actual frequency of 36.74 kHz. Figure 4 shows the (VI) characteristics chart for the given system. It is subdivided into four different regions; 1-Townsend or predischarge, 2-normal glow, 3-abnormal glow, and 4-discharge to arc transition.[30] The first region, namely, dark or Townsend discharge occurs prior to ignition. In the first region, a limited increase in the current proportional to the voltage is observed. In the second region, after the ignition of plasma, the voltage drops immediately. The negative slope in region 2 (Figure 4) shows voltage drop usually appears in microdischarges.[31] At lower pressure (vacuum), Schutze[30] observed no voltage increase after region 2 with increase in current. The authors

dx.doi.org/10.1021/ef301981f | *Energy Fuels* 2013, 27, 2748−2761

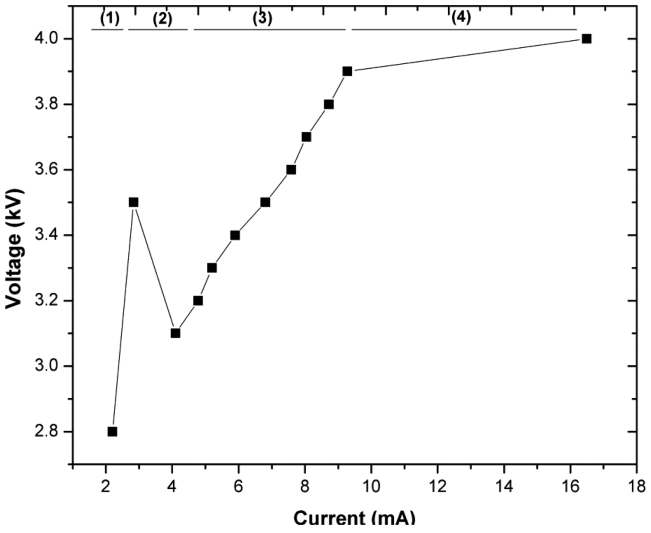

Figure 4. Current−voltage (VI) characteristic of AC powered DBD-corona hybrid discharge.

have reported rather a straight line parallel to increase in the current (Figure 2 in ref 30). However, at higher pressure, the second and third region may shrink, (voltage starts increasing immediately after second region),[30] which is the same behavior in the current study. In the third region, voltage again starts to increase with increasing the current until region 4 where a sharp decrease in the voltage is observed, which makes plasma highly conductive and leads toward discharge to arc transition.[30] Arcing is not desirable in the current studies; so, voltage was only increased until 4 kV. It is worth mentioning here that Schutze[30] has used DC glow discharge, whereas an AC powered DBD plasma is discussed in the current study. Principally, the direct current glow discharge does not resemble the radio frequency (Rf) plasma; the reason is the nature of the electric field distribution in a DC glow discharge, which is not time dependent. However, it is worth noting that the difference between DC plasma and RF plasma is not significant in a bulk at a high pressure.[32] From Figure 4, it is also clear that the minimum breakdown voltage for steam flowing at 1 atm in a discharge gap of 1.24 mm is 3.5 kV at 3 mÅ. This corresponds to a power of 10.5 Watts. This breakdown voltage is in agreement with the discussion done by Fridman.[9] Looking at the value of breakdown voltage of air, 30 kV/cm at 1 atm, it may be expected for water to breakdown at much greater voltage due to the density difference between air and water. However, a large number of studies have shown that the breakdown voltage of water is of the same order as for air. This is because of fast formation of gas channels in the body of water under the effect of high electric field.[9] This is a practically important effect that could be elucidated based on the process occurring at the electrode surface. The process occurring at the electrode surface can be further divided into two processes.[33] The first process is subdivided into two phases as well. In the first phase, a bubble is formed due to vaporization of liquid from the local heating in the strong electric field regions at the tip of electrode. In the second phase, electronic process, the breakdown occurs due to ionizing collision of electrons on their way across the breakdown gap. The first phase is not applicable in the current study as the water is already fed in the vapor phase. Since water is fed in the vapor phase, which provides an extra energy (latent heat of vaporization of water), an overall energy for water breakdown by plasmolysis is reduced. The second process is related to the underwater electrical discharges and arc formation and hence not applicable in the current study. Although, experimentally determined minimum breakdown voltage is 3.5 kV with current of 3 mÅ, the analysis is conducted at 4 kV to obtain a better data set. The corresponding current at 4 kV was 16 mÅ.

3.2. Plasma Optical Characterization. Figure 5 shows the spectra obtained by fiber optic probe from steam plasma. The

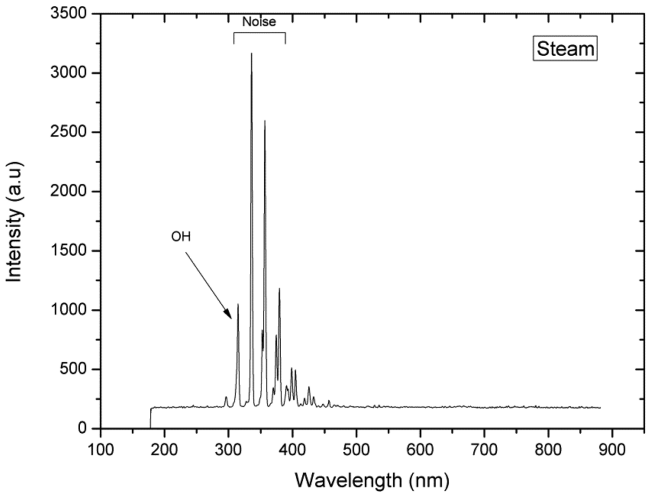

Figure 5. Spectrum of steam plasma.

spectrum shows OH band between 302 and 317 nm. It is observed that some peaks in the spectral region 300−400 nm, other than the peaks of OH band (302−317 nm), resemble nitrogen peaks (both second positive system of N_2 and first negative system of N_2^+) in this area.[34] However, those peaks have appeared in every experiment (spectral data of steam plasma, steam and argon plasma, and steam and nitrogen plasma), prompting an investigation of their identity, which is discussed in section 4. Figure 6 shows the spectrum of steam and argon plasma. A sharp increase in OH band (302−317) is observed, which is explained in section 3.3. In the same sense, the collision−radiative recombination of argon with the energetic electrons has also resulted in forming argon atoms in various excited states, which is illustrated by the increased

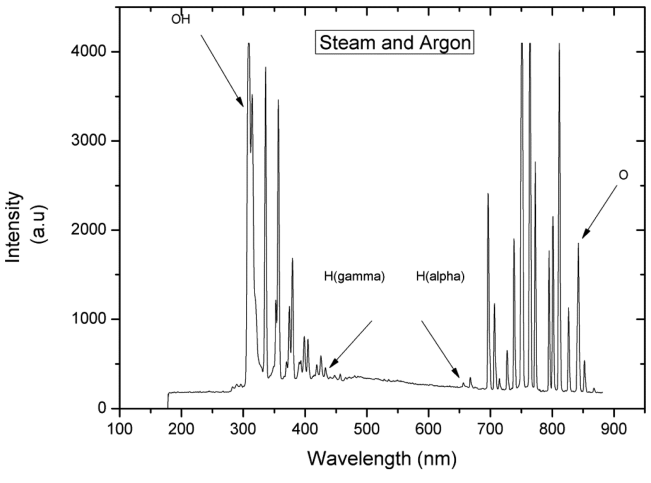

Figure 6. Steam and argon plasma spectrum.

dx.doi.org/10.1021/ef301981f | Energy Fuels 2013, 27, 2748−2761

intensity of the argon emission lines at 696.5 nm, 750.38 nm, and other argon lines in the near IR region. Nitrogen was introduced along with steam to determine the rotational temperature and vibrational temperature. Figure 7 shows the

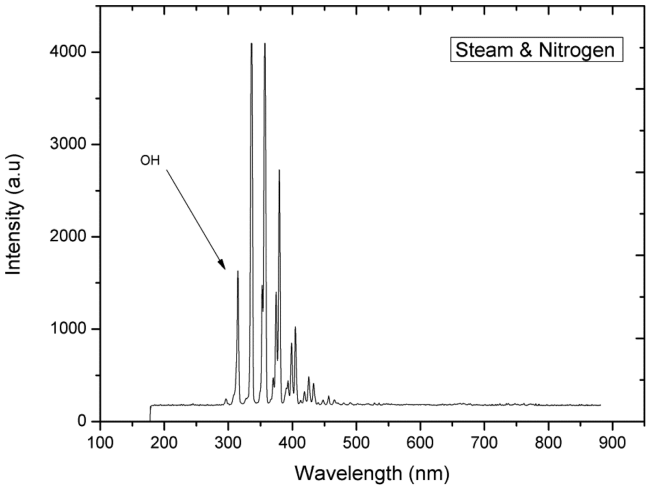

Figure 7. Steam and nitrogen plasma spectrum.

spectrum of steam and nitrogen. Along with OH (302−317 nm), nitrogen peaks are observed for both second positive system of N_2 and first negative system of N_2^+.[34] Spectral data from Ar(I) lines, OH band (302−317 nm), and second positive system of N_2 are used to calculate T_e, T_{exc}, T_{rot}, and T_{vib}. Figure 6 shows the abundance of Ar lines in the spectrum. These lines have reliable published values of transition probabilities and the energy gap between emitting upper levels is expanded within a range of more than two electron volts (eV), which is very important in choosing the lines for plasma diagnosis. The number of available Ar lines also gives an additional advantage of choosing (at expense of lower intensity signal) lines with biggest energy difference between upper energy levels. This energy gap is essential to achieve higher accuracy for using the traditional Boltzmann plot.[35]

Electron density is inferred by the formula $n_e = J/ev_d$ where n_e, J, e, and V_d represent the electron density ($1/m^3$), plasma current density ($Å/m^2$), electron charge, and electron drift velocity (m/s)). Electron drift velocity was measured by $vd = \mu \times E$ where, μ is electron mobility and E is applied electric field. The electric field was measured by using high voltage probe and digital oscilloscope (ADC-212 from Pico Technology Limited). The voltage was measured to be 4 kV dissipating across a gap of 1.24 mm producing electric field of 4.83×10^6 (V/m). Electron mobility was considered to be 0.01 ($m^2/(V - s)$).[29] This produces a drift velocity of 4.83×10^4 (m/s). Plasma current was measured using a validated digital current clamp meter (UNI-T, UT 201), where the current value is taken very near to the load and found to be 16 mÅ for the above given voltage value. Current density, 912 $Å/m^2$, was then measured by dividing the current with the electrode cross sectional area. Putting, the values of current density, electron charge, and drift velocity n_e was calculated 1.765×10^{17} m^{-3}, which is in agreement with other researchers.[29,36]

In nonlocalized thermal equilibrium (LTE) plasmas, a normal Boltzmann plot is not permitted because the deviation from equilibrium may occur by a factor of 1000. However, there still exists information about the temperature in line intensities in a more complex way.[37] It becomes very important to modify Boltzmann plot for estimation of T_e under non-LTE conditions. Electron temperature has been calculated under non-LTE conditions as follows:[29,35,37]

$$\ln\left(\frac{I_{ij}\sum A_{i>j}}{h\upsilon_{ij}A_{ij}b_{1i}}\right) = \frac{-E_i}{kT_e} + D$$

where T_e is the electron temperature, $h\nu_{ij}$ is the energy gap, k is Boltzmann constant, A_{ij} is the transition probability, and b_{1i} is a parameter determined by $b_{1i} = E_i^a \times p_i^b$. a and b are the fitting parameter obtained taken from Gordillo-Vázquez.[35] p_i for each level is given by the formula $p_i = (E_H/(E - E_i))^{1/2}$. E_H is the Rydberg constant (13.6 eV); E_∞ and E_i are the ionization energy and excitation energy of the excited state i. The sum of transition probabilities ($A_{i>j}$) should contain all the excited energy level and a number of radiative transitions starting in each considered argon energy level. Figure 8 shows the

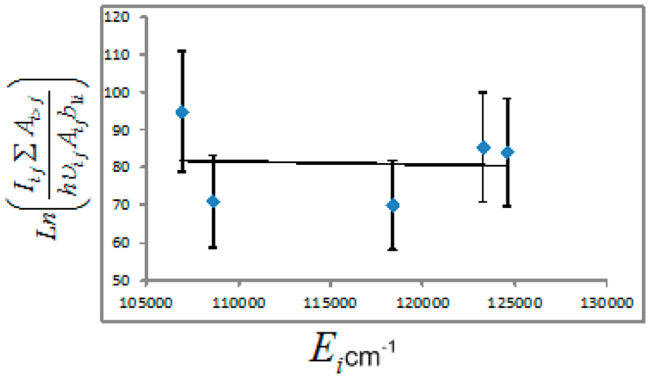

Figure 8. Modified Boltzmann plot for determination of electron temperature.

modified Boltzmann plot used to determine the electron temperature. T_e could be extracted from the slope of such modified Boltzmann plot. It is common that strong lines are originated from a relatively small energy band and spectroscopic energy system, which limits the energy difference between upper energy levels. This increases the errors in the determination of electron temperature. To avoid this, lines were chosen such that the gap between upper energy levels is greatest but at the cost of lower intensity signal. The data in the modified Boltzmann plot shows some disparity. Therefore, error bars of ±20% has been assigned to derive the electron temperature, which is in agreement with ref 35. The line produces a slope of −0.00007, which is equivalent to $-0.625/T_e$, which produces T_e = 8928.5 K = 0.77 eV.

The Debye shielding length is the characteristic length scale in plasma. This parameter serves as a length scale to shield the Coulomb potential of individual charged particle when they collide. It is calculated from the formula $\lambda_{De} = (\varepsilon_0 T_e/en_0)^{1/2}$ or λ_{De} (cm) $\approx 743(T_e/n_e)^{1/2}$,[38] where T_e and n_e are electron temperature and electron density, respectively. In the current study, it is found to be 3.24 μm, which is in agreement with ref 39.

It is well-known that temperature measurements based on optical emission spectroscopy are dependent on the relative intensities of the same atom. These measurements can also be based on those of the ions of neighboring ionization stages on the relative continuum intensities and on the relative absolute intensities among others. The excitation temperature (T_{exc})

dx.doi.org/10.1021/ef301981f | Energy Fuels 2013, 27, 2748−2761

Table 1. Spectrometric Data of the Argon

line	λ_{ij} (nm)	A_{ij} (s^{-1})	E_i (cm^{-1})	g_i	I_{ij} (a.u.)	ln $(I_{ij}\lambda_{ij}/g_iA_{ij})$
ArI	727.29	1.83×10^6	93 750.59	3.0	632.020	−2.480
ArI	738.39	8.47×10^6	107 150.05	5.0	1903	−4.508
ArI	750.38	4.45×10^7	95 399.82	3.0	4083.09	−3.774
ArI	763.61	2.45×10^7	106 102.71	5.0	4095	−3.668
ArI	794.18	1.86×10^7	94,553.66	1.0	1778.51	2.577
ArI	811.53	3.31×10^7	105 377.64	7.0	4095	−4.244

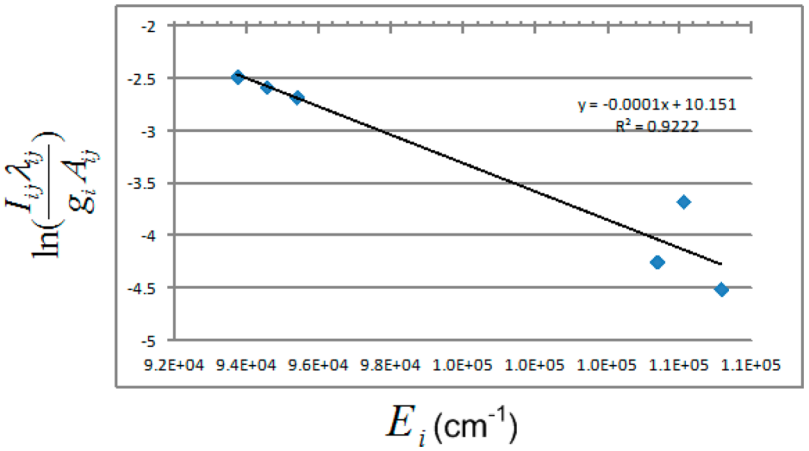

Figure 9. Boltzmann plot to determine excitation temperature.

depicts the population of the excited atomic states assuming that this follows Boltzmann distribution. It is a measure of the excitation capacity of atoms within the plasma. T_{exc} was measured in non-LTE conditions by Boltzmann plot method.[40] This method is particularly considered appropriate because it does not require a standard source of calibration, but a maximum energy area should be covered to increase the accuracy. The Boltzmann plot method is expressed by the following equation.[2,40]

$$\ln\left(\frac{I_{ij}\lambda_{ij}}{g_iA_{ij}}\right) = \ln K - \frac{E_i}{K_bT_{exc}}$$

where I_{ij} is the line intensity, λ_{ij} is wavelength, g_i is the statistical weight of the upper atomic state, A_{ij} is the transition probability, E_i is the excitation energy, k_b is the Boltzmann constant, and K is constant for all considered lines. The data used to obtain the Boltzmann plot are shown in Table 1. A plot is drawn between $\ln(I_{ij}\lambda_{ij}/g_iA_{ij})$ and E_i, which produces a slope $(1/K_bT_{exc})$, which is equal to $-0.625/T_{exc}$ and inversely proportional to the excitation temperature. Figure 9 shows the typical Boltzmann plot, which produced a slope of −0.0001, hence producing T_{exc} = 6250 K (0.53 eV).

The rotational temperature (T_{rot}) depicts the population of the rotational levels in the molecular species present in such discharge zone.[41] Rotational temperature is considered to be the closest to the gas temperature as the rotational relaxation is fast at atmospheric pressure.[42] The Boltzmann plot method could be applied in LTE plasma and also non-LTE plasma, provided the pressure is sufficiently high (as in the current study) so that the collisional frequency of molecules is higher than that of the radioactive decay probability of excited state under consideration, which leads toward thermal equilibration of the state population.[43] T_{rot} is measured by using rotational fine structure of electronic band such as $B^2\sum_u^+ - X^2\sum_g^+$ for N_2^+ (first negative system) and $A^2\sum^+ - X^2\prod$ for OH. The intensity of such rotational line for a transition $(J'-J'')$, then, could be expressed as a function of oscillator strength S_j or the transition probability, A_j:

$$I = DA_jh\upsilon \exp\left[\frac{-B_vhcJ'(J'+1)}{kT_{rot}}\right] \quad (A)$$

$$I = DS_j\upsilon^4 \exp\left[\frac{-B_vhcJ'(J'+1)}{kT_{rot}}\right] \quad (B)$$

where h is the Planck's constant, k is Boltzmann constant, B_v is the rotational constant that belongs to the vibrational quantum number v, and υ is the wavenumber associated to the emission line, where $S_j = K' + K'' + 1$. The practical values of S_j and $K' + K'' + 1$ is usually articulated as a function of the quantum number K'' (assigned to lower state). For N_2^+, two branches could be used, the P and the R branch.[44] For P branch, it is expressed as $K' = K'' - 1$ and $K' = K'' + 1$ for R branch. T_{rot}, then, could be calculated by plotting the intensity of the given line versus K''.[44]

$$\text{For } P \text{ branch, } \ln\frac{1}{2K''} = C - \frac{Bhc}{kT_{rot}}K''(K''-1) \quad (C)$$

$$\text{For } R \text{ branch, } \ln\frac{1}{2(K''+1)} = C - \frac{Bhc}{kT_{rot}}(K''+1)(K''+2) \quad (D)$$

where C is a constant value. The slop of such plot is equal $-Bhc/kT_{rot}$, which is equal to $-2.983/T_{rot}$; thus, T_{rot} can be estimated. The corresponding values of oscillator strength were taken from ref 44 and R branch was used to calculate the rotational temperature from the first negative system of N_2^+.

dx.doi.org/10.1021/ef301981f | Energy Fuels 2013, 27, 2748−2761

The data used for calculating T_{rot} are presented in Table 2. Figure 10 shows the graph between $(K'' + 1)(K'' + 2)$ and $\mathrm{Ln}[^1/_2(K'' + 1)]$, which produced a slope of −0.004 resulting in T_{rot} = 745.75 K = 0.064 eV.

Table 2. Spectrometric Data Used for the Calculation Rotational Temperature by N_2^+ Second Positive System

λ (nm)	I (a.u.)	K″	(K″+1)(K″+2)	Ln[$^I/_2$(K″ + 1)]
390.49	360.42	6	56	3.24
390.4	358.55	7	72	3.10
390.29	358	8	90	2.99
390.19	351	9	110	2.86
390.08	348	10	132	2.76
389.97	348	11	156	2.67
389.85	344	12	182	2.58
389.73	334.17	13	210	2.47
389.33	317.33	16	306	2.23

The OH spectra could also be used to determine T_{rot}. However, it is more complex having five main branches *O*, *P*, *Q*, *R*, and *S*. The whole band of OH $(A-X)$ transition could be used for determination of rotational temperature or more easily relative intensities of two groups of lines relating to the *R* and *P* branches could be utilized as well.[42] Again, eq A can be used, and T_{rot} can be calculated by plotting $\mathrm{Log}(I\lambda/A)$ versus *E*. The slope of such plot is given as $-0.625/T_{rot}$. The corresponding values of *A* and *E* are taken from ref 44. The data used for the calculation of T_{rot} from OH are given in Table 3. Figure 11 shows the plot of the following equation:

$$\log(I\lambda/A) = \frac{-E}{kT_{rot}} + D$$

where *D* is a constant value. The estimated value of the slope is -8×10^{-4}, which produced

$$T_{rot} = 781.2\ \mathrm{K} = 0.067\ \mathrm{eV}$$

Molecular band of the second positive system of N_2 and first negative system of molecular ion of nitrogen N_2^+ can be utilized to calculate vibrational temperature T_{vib}. In the current study, T_{vib} is calculated using the second positive system of N_2 by considering the nonthermal equilibrium conditions.[45] The method to obtain T_{vib} is based on the emission process; $N_2^+(B^2\sum_u^+) \rightarrow (X^2\sum_g^+) + h\nu$, where the mechanism for

Table 3. Spectrometric Data Used for the Calculation of Rotational Temperature from OH

λ_{ij} (nm)	branch	$A_{ij} \times 10^8$ (sec^{-1})	E (cm^{-1})	I_{ij} (a.u.)	Log(Iλ/A)
308.405	R_2	2.70	32542	4095	−2.32
308.023	R_2	5.70	32643	4095	−2.65
307.703	R_2	8.90	32778	3905.8	−2.86
307.437	R_2	12.8	32947	3753.6	−3.04
306.918	R_2	24.8	33650	3927.1	−3.38

production of molecular ions in the state of $N_2^+(X^2\sum_g^+)$ is direct ionization by electronic impact of fundamental state $N_2(X^1\sum_g^+)$ Plotting a graph between $\ln[I_{v',v''}\lambda_{v',v''}/A_{v',v''}hc]$ versus vibrational term $G_{(v)}$produces a slope of $-hc/k_bT_{vib}$, from where T_{vib} could be calculated. Where $I_{v',v''}$ is the intensity of the vibrational band (v',v''), $\lambda_{v',v''}$ is the corresponding wavelength, $A_{v',v''}$ is Einstein's coefficients for spontaneous emission, $G_{(v)}$ is vibrational term, *h* is Planck's constant, and *c* is the speed of light.

A graph can be plotted between $\ln[I_{v',v''}\lambda_{v',v''}/A_{v',v''}hc]$ and $G_{(v)}$, which produced a slope of hc/k_bT_{vib}. The data used are shown in Table 4.

Figure 12 shows the plot between $\ln[I_{v',v''}\lambda_{v',v''}/A_{v',v''}hc]$ and $G_{(v)}$ producing a slope of -2×10^{-5} hence $-2.0 \times 10^{-5} = hc/k_bT_{vib} \Rightarrow T_{vib} \approx 720.2$ K.

The results of the temperature measurement are summarized in Table 5. T_{rot}, which is measured by first positive system of N_2 and OH band does not differ by much.

It is known that the vibrational temperature value exists in the range between gas temperature and electron temperature.[46] Often gas temperature could be inferred from the rotational temperature of the excited molecules, which have the time to equilibrate with the gas molecules of plasma before photon emission, hence their rotational distribution could reflect that of the gas molecules in the plasma.[47] However, it is interesting to note that, in the current study, the rotational temperature is found to be a bit higher than the vibrational temperature. There could be a couple of explanations for this anomalous behavior. First, current study plasma has been generated at atmospheric pressure. It is known that rotational temperature remains constant with an increase in the pressure. However, vibrational temperature is found to decrease with increasing pressure.[47,48] Second, a presence of even a small amount of oxygen in the plasma is known to lower the vibrational temperature at any point in the discharge zone. This could be explained on the

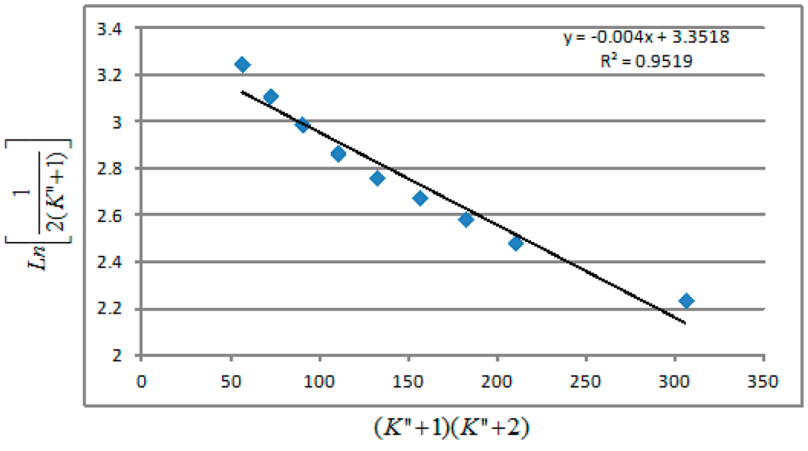

Figure 10. Linear fit between $(K'' + 1)(K'' + 2)$ and $\mathrm{Ln}(^I/_2(K'' + 1))$ to calculate rotational temperature.

dx.doi.org/10.1021/ef301981f | Energy Fuels 2013, 27, 2748−2761

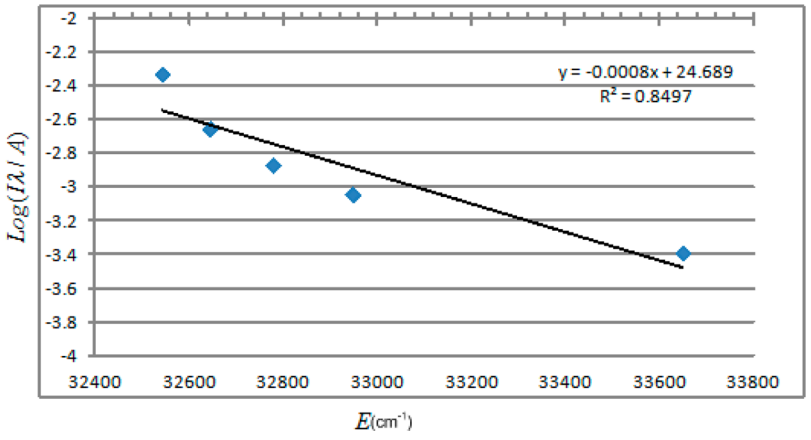

Figure 11. Linear fit to calculate the rotational temperature from OH.

Table 4. Spectrometric Data Used for the Calculation of Vibrational Temperature

(v',v'')	$I_{v',v''}$ (a.u.)	$\lambda_{v',v''}$ (nm)	$G_{(v)}$ (m^{-1})	$A_{v',v''}$ (s^{-1})	$\ln[I_{v',v''}\lambda_{v',v''}/A_{v',v''}hc]$
(0,2)	2050	380.37	2.63×10^{06}	3.53×10^{06}	55.36
(1,3)	1179.8	375.422	2.66×10^{06}	4.89×10^{06}	54.47
(2,4)	418	370.933	2.70×10^{06}	4.05×10^{06}	53.61
(3,5)	246	367.056	2.72×10^{06}	2.38×10^{06}	53.60

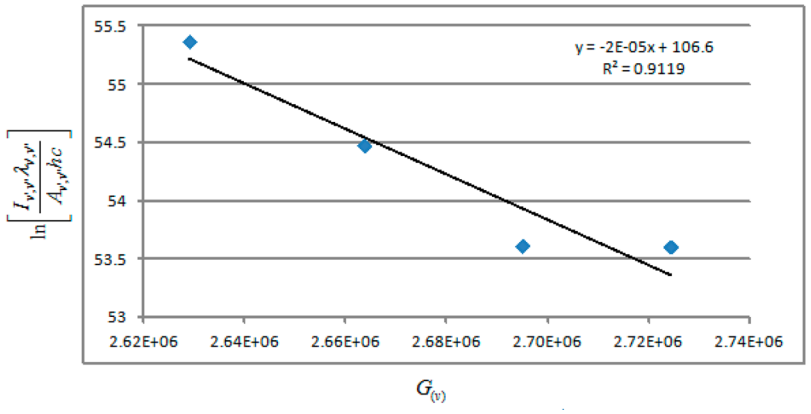

Figure 12. Linear fit to calculate vibrational temperature from N_2^+ second positive system.

Table 5. Summary of Plasma Characterization

electron density	1.765×10^{17} m^{-3}	
debye shielding	3.24 μm	
temp	K	eV
electron	8928.57	0.77
excitation	6250	0.53
vibrational	720.217	0.062
rotational		
N_2^+ based	745.75	0.064
OH based	781.21	0.067

basis of higher rate coefficient of relaxation between vibrational and rotational/translational motions than nitrogen.[48] Since oxygen, in the current study, has been evidently generated, it could possibly result in decreasing the vibrational temperature. Both factors of having plasma at atmospheric pressure and generation of oxygen within plasma zone could explain this anomalous behavior. Also, water vapor, which was used as a feed in the current study, could give extra energy to the gas phase molecules in plasma zone, thereby increasing the rotational temperature.

3.3. Energy Yield and Cost. The amount of water vapor decomposed by plasmolysis was found by connecting two condensers to the outlet of the reactor. Second order central composite rotatable design was applied to monitor water vapor decomposition rate% (Y) as an objective function. This was done to establish a statistical model correlating the water vapor decomposition rate with a steam flow rate and argon flow rate. Steam flow rate and argon flow rate were studied as two parameters affecting the water vapor decomposition rate according to the following model:[28]

$$Y = B_0 + B_1x_1 + B_2x_2 + B_{11}x_1^2 + B_{22}x_2^2 + B_{12}x_1x_2$$

where B_0, B_1, B_2, B_3, B_4, and B_5 are the constants, (x_1) and (x_2) are the code value for steam flow rate (mL/min) and argon flow rate (mL/min). These code values are tested in the range $(-1.414, -1, 0, +1, +1.414)$, which is equivalent to values 1, 2, 3, 4, 5 mL/min of steam and 10, 20, 30, 40, 50 mL/min for argon, respectively. The data were fitted in the model equation

dx.doi.org/10.1021/ef301981f | Energy Fuels 2013, 27, 2748−2761

using a multiple stepwise regression analysis, which gave the following empirical model.

$$Y = 9.64 - 0.16x_1 + 0.28x_2 - 0.51x_1^2 - 0.11x_2^2 + -0.025x_1x_2$$

The average absolute error of the model obtained was estimated to be 1.32%. It was found that with the given experimental set up and power setting the water vapor decomposition rate was decreased with increasing steam flow rate at values higher than 2 mL/min, while an increase in the argon flow rate enhances the decomposition rate. In consequence, a maximum decomposition rate of 10% was found when applying 2 mL/min of steam and 50 mL/min of argon.

Concentration of H_2O_2 was measured by colorimetric method, which is based on a specific reaction between H_2O_2 and titanyl ions giving a stable yellow colored complex of pertitanic acid, which gives an absorption peak at λ = 410 nm.[49]

$$Ti_4 + +H_2O_2 + 2H_2O \rightarrow TiO_2 + H_2O_2 + 4H^+$$

There was no H_2O_2 found to produce in the experiment, as there was no change in color observed, which evidently showed there is no formation of pertitanic acid and hence no H_2O_2. Similar results were observed by Givotov,[5] in which H_2 and O_2 were produced in similar stoichiomertric ratios.

Both vapor and liquid phases were analyzed by gas chromatography (GC). Liquid samples were collected at the end of experiment. Bottles containing liquid sample were kept in water bath at 70 °C for half an hour before taking the sample. A 10 mL standard plastic syringe was used to collect samples from head space. Samples were directly injected into GC (Varian CP3800 fitted with thermal conductivity detector (TCD), 2m HAYESEP C), where an argon was used as a carrier gas. There was no peak observed for hydrogen or oxygen. Hence, hydrogen and oxygen produced from the experiment were not dissolved in the steam condensate, that is, negligible as the solubility of oxygen and hydrogen in water at 100 °C is negligible.

Steam leaving reactor was condensed via condenser and then collecting the gases at the condenser outlet using a standard gas sample bag. Samples collected were fed to the above-mentioned GC. Gas chromatography analysis showed very little percentages of H_2 (0.02306%) and O_2 (0.5195%). However, when samples were collected from condenser top, oxygen and hydrogen concentrations rose to 5.4213% and 0.0438%, respectively.

It is worth noting that the reactor internal volume is about 5 × 10^{-4} L. In consequence, attaching any container directly at the reactor outlet section is likely to increase the pressure inside the reactor and hence change reaction kinetics. Since there was a large volume exists in the condenser, the gases were prevented from entering the gas sampling bag because of pressure drop built up at the small orifice of bag inlet. Moreover, the sampling bag was unable to preserve the hydrogen, as a continuous decrease in the hydrogen percentage was observed when samples from the same bag were analyzed over time interval of 30 min. One of the reasons behind the hydrogen concentration reduction is its low density. As it is lightest among other product gases (oxygen and argon), the analysis suggests that hydrogen might not flow at the same rate of other gases and kept at the condenser top section.

Bags (SKC bags) that could contain hydrogen for longer periods of time were then used to collect gases. Bags were attached directly at the outlet of the reactor. This was done to collect all the gases and condense steam directly in the bag to eliminate the possibility of hydrogen or oxygen staying behind in the condenser section. The bag was submerged in a cold trap (thermal box containing ice, water, and salt) to avoid overheating and help condensing the steam. The experiment was run for 3 min with 2 mL/min of steam and 50 mL/min of argon gas. The gas samples from the bag were withdrawn and fed to the GC. The percentage of oxygen was dropped to 0.560%; however, the percentage of hydrogen remained constant. The bag has got a small orifice and only one turn opening is usually advisable by the company, so it leaves very little space for the gases to leave the reactor and fill the bag. The smaller orifice has created pressure inside the reactor; this was partially indicated from a sound of pressure relief when SKC bag was detached from the reactor at the end of experiment. The pressure build up led to changes in the whole reaction kinetics and hence percentage of oxygen was found to be very low. It was questionable whether the sampling bag inner surface is the reason behind oxygen concentration reduction or not? This was checked by filling the sampling bag with a standard mixture of 1% H_2, 5% O_2, and 94% Ar for a day. GC showed no decrease in the percentage of oxygen when analyzed after 1 day. The experiment repeated three times and showed similar results.

Considering the pressure build up in the reactor, a long glass (1.5″ × 15″) tube was used as a collection vessel. A rubber bung was used to seal the tube with a 8 mm hole serving as inlet. The tube was submerged in a cold trap for condensing the steam. Experiment was run for 3 min. GC showed 19.0532% oxygen, though hydrogen was dropped to 0.0799%. The experiment was repeated, and similar results were obtained. Since the inlet section of glass tube was almost similar to the outer diameter of reactor, gases would have flown easily without building any pressure in the reactor. This may explain the higher percentage of oxygen obtained. However, the glass tube had a fixed volume, and it was airtight; therefore, it was difficult to collect samples from it. This led to use of a glass syringe, which can be connected to the reactor directly, and is likely to have a little friction between its inner surface and plunger. Accordingly, no pressure was created inside the reactor.

Two glass syringes of 20 and 100 mL were used to collect the gases. The experiment was finished when the glass syringe was full (15 s for 20 mL and 52 s for 100 mL). The gases did not fill very smoothly in the syringes; they were rather filled in time intervals creating pressure in the reactor. GC showed an average of 14.65% oxygen and 0.308% hydrogen.

It can be concluded that the percent of hydrogen and oxygen and overall volume gases collected are dependent on the used methodology, and hence, it is difficult to quantitatively analyze the experiments.

For inline detection, reactor was connected to GC through flexible tubing. The GC used is a Perkin-Elmer Autosystem XL, while the column is an RT-M sieve 5A (30 m × 0.53 mm inner diameter) by Restek. Nitrogen gas was used as a carrier gas. This implied no oxygen could be detected and a better sensitivity toward H_2 because sensitivity increases if the difference between thermal conductivity of carrier gas and sample gas is high.[50] Calibration was done for 1%, 5%, 10%, and 20% of hydrogen in nitrogen. GC analysis showed that

about 0.9% of hydrogen with no oxygen was produced compared with values obtained via other methodologies.

Two different GCs fitted with TCD have been used to analyze hydrogen. No hydrogen or oxygen could be found in the samples collected from head space. Again, GC analysis showed that percentages of hydrogen and oxygen could be varied according to the gas collection method.

It becomes obvious that different methods create different level of pressures inside the reactor, which changes the kinetics and hence changes different percentages of hydrogen and oxygen shown by GC. Stoichiometrically, there should be half a mole of oxygen per every mole of hydrogen produced and hence similar volumetric ratios. The stoichiometric ratios between hydrogen and oxygen shown by GC analysis do not match with this theory. It could be explained on the basis that hydrogen is produced in the experiments; however, and because of a small size molecule, it might have escaped during collection. Due to high temperature and pressure involved in the experiments, a lot of hydrogen gas produced might have escaped while collecting the gas.

It is noted that hydrogen generation studies such as Porter[51] and Burlica,[10] have successfully quantified hydrogen production by GC analysis. However, their studies involved liquid water, hence less pressure to deal with.

Considering the preceding discussion, hydrogen was quantified using indirect methods that are amount of hydrogen produced was determined by monitoring the decomposition rate of water vapor.

To find the water vapor decomposition rate, plasma was ignited with water vapor without argon. Decomposition rate was calculated by monitoring the difference in volume that collected after plasma ignition during a period of time.

$$\text{decomp. rate (\%)} = \frac{\text{vol. water vapor decomp.}}{\text{operation time}} \times 100$$

Considering the results from the model, water vapor flow rate was set to be 2 mL/min, which produced a decomposition rate of 5%. Cost and energy yield has been calculated considering two cases: (1) 5% decomposition rate of pure water vapor flows at 2 mL/min and (2) 10% decomposition rate of a mixture contained water vapor flows at 2 mL/min and argon at 50 mL/min. Amount of hydrogen produced is calculated stochiometrically considering 5% and 10% decomposition of steam in both cases. The power is measured to be 3.960 KJ/min (4×10^3 V $\times$ 16.5 $\times$ 10^{-3} Å). The cost (7.3 Pence/kWh) is taken as all consumers average from Quarterly Energy Prices.[52] Hydrogen energy yield (g/kWh) in both studied cases and cost for 1 m^3 of hydrogen produced/kWh and £/kWh energy produced by hydrogen is given in Table 6. It is evident from Table 6 that in presence of argon the decomposition rate is doubled. The increase in decomposition was reported by Burlica[10] as well. This result is attributed to collisions of the argon excited species (Ar (^{3}P)) with water molecule. Ar (^{3}P) is produced by electron impact collision with argon atoms. Ar (^{3}P), hence produced, collide with water molecules, and these collisions leads to efficient dissociative excitation of the water molecules,[53] which consequently produces extra OH radicals, as demonstrated by the increased intensity of OH emission lines (302−317 nm) in Figure 6.

Table 6. Amount of the H2 Produced, Energy Yield, and Price of H_2 Produced

feed	decomposition rate (%)	amount of H_2 produced (gm/min)	price (m^3 of H_2/kWh)	price (£/kWh)
steam	5	0.011	0.153	0.18
argon + steam	10	0.022	0.306	0.09

$$\text{Ar} + e \rightarrow \text{Ar}(^3\text{P}) + e \quad (1)$$

$$\text{Ar}(^3\text{P}) + \text{H}_2\text{O} \rightarrow \text{H} + \text{OH} + \text{Ar} \quad (2)$$

Energy efficiency of the process is defined as a ratio of the amount of energy produced by unit of fuel to the amount of energy required to produce the fuel. Considering 1.4×10^5 kJ/kg as gross calorific value (GCV) of H_2, energy efficiency was calculated by taking the ratio of amount of heat that would be generated by H_2 produced in the experiment to the amount of heat, which was used to produce H_2 and presented in Table 7.

$$\text{energy efficiency} = \text{energy produced by unit amount of } H_2 \text{ /energy consumed to produce unit amount of } H_2 \times 100$$

Table 7. Energy Yield, Energy Efficiency and Thermodynamic Efficiency of H_2 Production by Plasmolysis

feed	energy yield (g/kWh)	energy efficiency (%)	thermodynamic efficiency (%)
steam	10	39.39	39.62
argon + steam	20	78.77	79.16

The other type of efficiency usually defined as the thermodynamic efficiency, which is the ratio of theoretical amount of energy to produce unit of fuel to the experimental amount of energy spent.

$$\text{thermodynamic efficiency} = \text{theoretical amount of heat required to break } H_2O \text{ /experimental amount of heat spent to break } H_2O \times 100$$

The thermodynamic efficiency was calculated to be 39.62% for steam plasmolysis and 79.16% for steam plasmolysis along with argon gas.

$$\text{H}_2\text{O} \rightarrow \text{H}_2 + \frac{1}{2}\text{O}_2 \quad (3)$$

The data in Table 8 are taken from Burlica.[10] Comparison of energy yields for hydrogen production for different types of plasma processes and other hydrogen producing technologies is given. In the current study the energy yield of steam plasmolysis in a DBD-corona hybrid reactor is equal to the microwave discharge. It is worth noting that the energy yield of steam plasmolysis with an argon gas is equal to electrolysis. Depending on the use of hydrogen, the argon gas used can be recycled. If the hydrogen is to be used in the plant as an intermediate energy storage, then conversion occurred in the fuel cell will result in purging argon in the off gases, hence naturally separated and recycled. If the hydrogen is to be used as a chemical intermediary, say for reducing biofuels to drop-in

dx.doi.org/10.1021/ef301981f | Energy Fuels 2013, 27, 2748−2761

Table 8. Hydrogen Energy Yield for Kinetic and Thermodynamic Limits for Different Types of Plasmas Processes and Other Technologies Producing H_2[10]

method	H_2 (g/kWh)	ref
thermodynamic limit	25−30	9
Kinetic Limit		
absolute quenching	5.2	
ideal quenching	10	
super ideal quenching	13	
electrolysis	20	10
	14−18	
photocatalysis	0.01	
microwave plasma	10	9
corona	2	10
AC gliding arc	1.3	
glide arc spray (Ar as carrier gas)	13	
DBD−Corona Hybrid reactor		
steam only	10	current study
steam and argon	20	current study (best case)

fuels, then if it is a liquid drop in fuel, the argon will stay in the gaseous phase and again recycled automatically.

The other high energy yield process is the glide arc spray using argon as carrier gas.[10] Those authors used water droplets. However, in the current study, a low quality steam was used instead. The current study is envisaged to utilize waste heat, which is widely available in the chemical engineering industries and power plants. Usually the exhaust temperature from most industrial processes and power plants are lower than 370 °C. Recovering this heat by the usual methods of waste heat recovery is economically infeasible and releasing this heat into the atmosphere causes heat pollution.[54] Such heat could easily be recovered to produce low quality steam (approximately 1 atm and 100 °C), thus increasing process efficiency and preventing heat pollution. This low quality steam could then be converted to hydrogen by plasmolysis.

The thermodynamic limit of reaction 1 is 28.7 g/kWh (2.6 eV/molecule) with a kinetic limit of absolute quenching, ideal quenching, and super ideal quenching of 5.2, 10, and 13 g/kWh, respectively.[9] It is interesting to note that in the current study when applying steam and argon, the kinetic limit has exceeded the values reported in the literature. This is possible because the theoretical kinetic limit of quenching process for thermal plasmas given in refs 9 and 10 is different compared with nonthermal plasmolysis at atmospheric pressure (current study). The logical explanation of high energy yield and higher efficiencies in the current study is the inclusion of latent heat of vaporisation (2257 kJ/kg) by utilizing the waste heat and relatively smaller flow channel, which enables water molecule dissociation at a relatively lower power. The flow channel diameter used in the current study was 1.24 mm; however, as mentioned earlier, Lozano-Parada and Zimmerman[25] have reported production of ozone at 170 V AC with a micro-channel plasma reactor of 800 μm diameter. Therefore, a significant reduction in the power requirement can be expected when using a flow channel in micrometer scale diameter. This is attributed to the fact that only a small potential difference is required to maintain high electric field strength across the channel as there exists an inverse relation between electric field strength and discharge gap. Miniaturizing plasma reactors also enhances the control over the process because the use of microfluidics can tailor fluid dynamics. The high but brief field gradients that exist in such plasma reactors are electronically controlled and spatially precise,[55] and hence, it can be concluded that further improvement in the efficiency is possible by better designing and optimizing reactions conditions.

It is worth nothing here that unlike large scale plasma reactors, power supplies for such plasma microreactors are miniaturized as well and available commercially at very low price (~$10). These plasma microreactors can also be ignited with battery sources.[56] These power supplies can be coupled with such plasma microreactor to produce hydrogen locally instead of large scale hydrogen generation at commercial plants and distributing it to the consumers. Hydrogen can be produced and delivered to the reactor, fuel cell, or combustor instantaneously. This becomes especially important for the use of hydrogen as transport fuel. In the light and heavy vehicles, this development could solve the "hydrogen storage issues", which is one of the biggest barriers of the hydrogen economy.[57]

4. IDENTIFICATION OF PEAK BETWEEN 317 AND 400 NM

The following section is dedicated to discuss the identity of the peaks in the spectral range 317−400 nm. As seen in Figures 5, 6, and 7, the peaks in the range 317−400 nm are always present irrespective of the gas or vapors in the system. These peaks appeared simply because of (1) N_2 in the system, (2) interaction of plasma with glass surface, or (3) formation of NH due to existence of nitrogen in the air and formation of hydrogen in the system. Petitjean and Ricard[58] have shown the formation of NH (λ = 336 nm) radical in the mixture of N_2−H_2 glow discharge for metal surface nitriding. The NH signal dominated the spectrum at lower concentration of H_2 with highest signal achieved at about 10% concentration. Since in the current study, a similar N_2/H_2 ratio is expected, it may be possible that a peak at λ = 336 nm appears in the spectrum because of NH formation.

A test was devised to eliminate the interactions with glass surface and to remove nitrogen from the system. A tube (9 cm inner diameter) is filled with water and two bungs were fitted at each end having two electrodes, as shown in Figure 13.

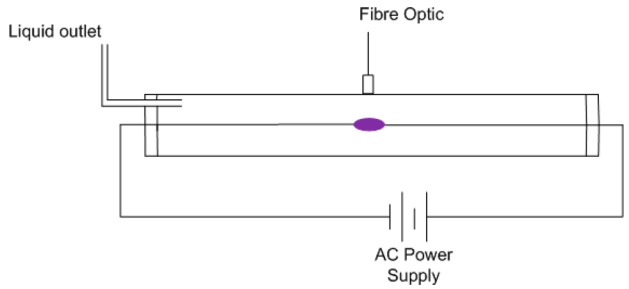

Figure 13. Plasma generated inside the water filled glass tube.

Interelectrode gap of approximately 1 mm was maintained. Since the system was nonflow, nitrogen cannot enter to the system. Solubility of nitrogen gas in water at room temperature (0.02g of N_2/kg of H_2O) is very low; hence, ideally, the amount of nitrogen in the system is relatively negligible. Plasma was initiated between the electrodes and signals were taken by UV−visible fiber optic probe. A pathway was provided to push the water outside the tube when products (H_2 and O_2, etc.) are

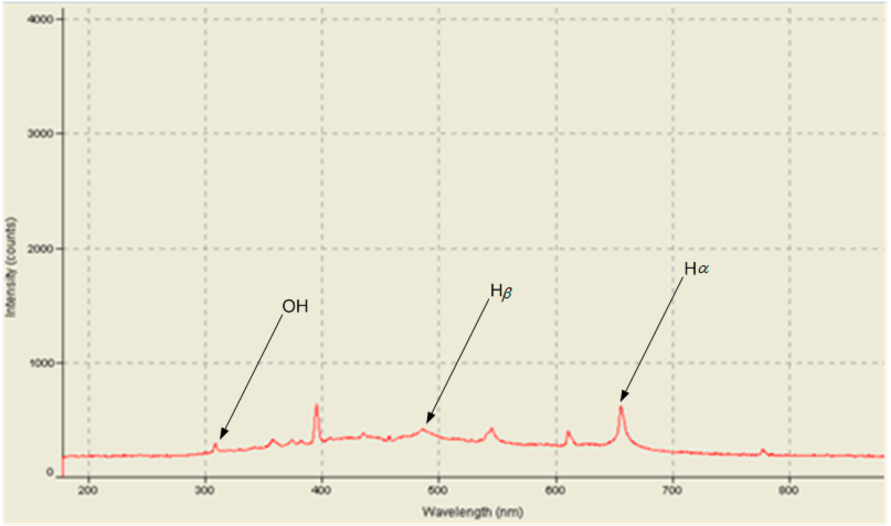

Figure 14. Spectrum of underwater plasma.

formed due to water plasmolysis. Plasma generated, in this case, is localized in the interelectrode gap, thus avoiding the contact between plasma and glass surface. The resulting spectrum is shown in Figure 14. It shows signals of H_α, H_β, and OH; however, no peaks in the range 317−400 nm were observed. This could be as a result of two reasons: (1) there was no contact of plasma with glass surface and (2) a negligible concentration of dissolved nitrogen in the water, which consequently results in no signal.

To explore the possible changes on the glass layer properties upon being subjected to plasma effects, the contact angle of a demineralized water droplet has been measured using the FTA tensiometer and applying sessile drop technique. The measurement applied for two glass slides: before and after being subjected to argon. Argon was set to 105 mL/min at 0.35 bar *g*. The power was set to 4 kV. The results show that the contact angle for a demineralized water droplet has increased from 56.3° to 103.35°, as shown in Figure 15, which indicates

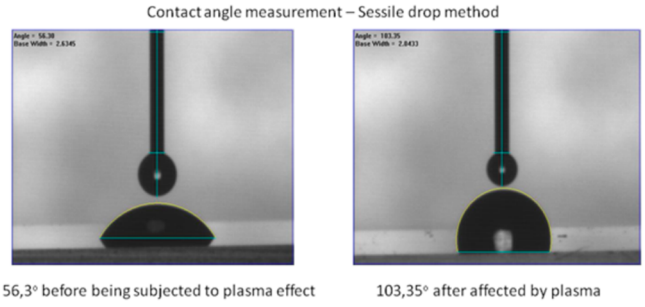

Figure 15. Contact angle of the slide before and after plasma treatment.

significant alterations on the surface properties due to plasma effect. Plasma effect leads to increase free radicals on the glass surface and the formation of polar compounds, which consequently causes considerable changes in the glass properties demonstrated by the increase in the surface wettability. This effect can change the nature of the glass surface from hydrophilic to hydrophobic. Li[59] has shown rise in the level of water by 6 mL in a capillary tube after plasma treatment, which shows the change of properties of glass from hydrophilic to hydrophobic. They reported that after one minute of operation, there was a difference of 38° (contact angle) between treated and untreated capillary. To sum up, It is possible that one of the above-mentioned interactions with glass surface caused these specific signals in the range 300−400 nm (other than OH band (302−317 nm)). Nonetheless, a detailed study is required to elucidate the appearance of these peaks, which is planned for a future work.

5. CONCLUSIONS

An experimental investigation is presented for the production of hydrogen from plasmolysis for two case studies: (1) pure water vapor and (2) water vapor and argon gas. The generated plasma has been characterized. Voltage and frequency output signal has been given to show the stability of signal and main frequency in the power output. VI characteristic chart has been given and discussed in detail. A minimum breakdown voltage of 3.5 kV, which dissipates 3 mÅ in the reactor at 1 atm, has been found experimentally for water vapors. Electron density, 1.765×10^{17} m^{-3} and Debye shielding 3.24(μm) has been calculated. Electron temperature, excitation temperature, rotational temperature, and vibrational temperature were calculated. Rotational temperature was calculated by both first positive system of N_2 (0.640 eV) and OH (0.067 eV) band. The temperatures estimated demonstrated the order $T_e(0.77) > T_{exc}(0.53) > T_{rot}(0.067)$, which confirms existence of non-LTE plasma bulk. Energy yield was calculated for both cases. Analysis based on the decomposition rate suggests that an energy yield of 10 g/kWh for water vapor and 20 g/kWh for water vapor and argon, which is on par with electrolysis. Energy efficiency and thermodynamic efficiency for water vapor plasmolysis along with argon was found to be 78.77% and 79.16%, respectively. Water vapor plasma was characterized by optical emission spectroscopy. A discussion is presented on the identification of peaks in the spectral range between (317−400 nm). Spectral data obtained from underwater plasma showed that no signal of the peaks between 320 and 400 nm exist, which denoted that either peaks are sensitive to contact of plasma with glass surface or presence of nitrogen gas in the system. Lastly, a contact angle differed by 42.95° after plasma treatment demonstrated that a significant alterations occurred in the surface properties of glass due to plasma treatment.

dx.doi.org/10.1021/ef301981f | *Energy Fuels* 2013, 27, 2748−2761

AUTHOR INFORMATION

Corresponding Author

*Tel: 00447556565337. Fax: 00441142227501. E-mail: cpp09fr@sheffield.ac.uk.

Notes

The authors declare no competing financial interest.

ACKNOWLEDGMENTS

Fahad Rehman acknowledges the COMSATS Institute of Information and Technology, Pakistan; The University of Sheffield, U.K.; and Professor William B. Zimmerman for a doctoral scholarship. Wameath S. Adbul-Majeed acknowledges the Iraqi Ministry of Higher Education and scientific research for a doctoral scholarship (2009−2012). William B. Zimmerman thanks the EPSRC for the financial support under the grant number (EP/IO27858/1).

REFERENCES

(1) Holladay, J. D.; Hu, J.; King, D. L.; Wang, Y. An overview of hydrogen production technologies. *Catal. Today* **2009**, *139* (4), 244−260.

(2) Ni, M.; Leung, D. Y. C.; Leung, M. K. H.; Sumathy, K. An overview of hydrogen production from biomass. *Fuel Process. Technol.* **2006**, *87* (5), 461−472.

(3) Dixon, R. K. Advancing towards a hydrogen energy economy: Status, opportunities, and barriers. *Mitigation and Adaptation Strategies for Global Change* **2007**, *12* (3), 325−341.

(4) Turner, J. A. Sustainable hydrogen production. *Science* **2004**, *305* (5686), 972.

(5) Givotov, V.; Fridman, A.; Krotov, M.; Krasheninnikov, E.; Patrushev, B.; Rusanov, V.; Sholin, G. Plasmochemical methods of hydrogen production. *Int. J. Hydrogen Energy* **1981**, *6* (5), 441−449.

(6) Maehara, T.; Toyota, H.; Kuramoto, M.; Iwamae, A.; Tadokoro, A.; Mukasa, S.; Yamashita, H.; Kawashima, A.; Nomura, S. Radio frequency plasma in water. *Jpn. J. Appl. Phys.* **2006**, *45* (11), 8864−8868.

(7) Koo, I. G.; Lee, W. M. Hydrogen generation by plasma-assisted electrochemical pumping. *Electrochem. Commun.* **2007**, *9* (9), 2325−2329.

(8) Nguyen, S. V. T.; Foster, J. E.; Gallimore, A. D. Operating a radio-frequency plasma source on water vapor. *Rev. Sci. Instrum.* **2009**, *80*, 083503.

(9) Fridman, A. *Plasma Chemistry*; Cambridge University Press: Cambridge, 2008.

(10) Burlica, R.; Shih, K. Y.; Locke, B. Formation of H_2 and H_2O_2 in a water-spray gliding arc nonthermal plasma reactor. *Ind. Eng. Chem. Res.* **2010**, *49*, 6342−6349.

(11) Rehman, F.; Lozano-Parada, J. H.; Zimmerman, W. B. A kinetic model for H_2 production by plasmolysis of water vapors at atmospheric pressure in a dielectric barrier discharge micro-channel reactor. *Int. J. Hydrogen Energy* **2012**, *37* (23), 17678−17690.

(12) Jasinski, M.; Dors, M.; Mizeraczyk, J. Production of hydrogen via methane reforming using atmospheric pressure microwave plasma. *J. Power Sources* **2008**, *181* (1), 41−45.

(13) Wang, W.; Zhu, C.; Cao, Y. DFT study on pathways of steam reforming of ethanol under cold plasma conditions for hydrogen generation. *Int. J. Hydrogen Energy* **2010**, *35* (5), 1951−1956.

(14) Mutaf-Yardimci, O.; Saveliev, A.; Fridman, A.; Kennedy, L. Employing plasma as catalyst in hydrogen production. *Int. J. Hydrogen Energy* **1998**, *23* (12), 1109−1111.

(15) Boutot, T.; Buckle, K.; Collins, F.; Fletcher, D.; Frontain, E.; Kozinski, J.; Lister, D.; Lin, H.; Liu, Z.; Mendoza, G. High-concentration hydrogen production from natural gas using a pulsed dielectric barrier discharge. *Proc. Hydrogen Fuel Cells*, Toronto, Canada, 2004.

(16) Mizuno, T.; Akimoto, T.; Ohmori, T. Confirmation of anomalous hydrogen generation by plasma electrolysis. *4th Meeting of Japan CF Research Society*, Iwate, Japan, 2002; pp 17−18.

(17) Chaffin, J. H.; Bobbio, S. M.; Inyang, H. I.; Kaanagbara, L. Hydrogen production by plasma electrolysis. *J. Energy Eng.* **2006**, *132*, 104.

(18) Sarmiento, B.; Brey, J. J.; Viera, I. G.; Gonzalez-Elipe, A. R.; Cotrino, J.; Rico, V. J. Hydrogen production by reforming of hydrocarbons and alcohols in a dielectric barrier discharge. *J. Power Sources* **2007**, *169* (1), 140−143.

(19) Paulmier, T.; Fulcheri, L. Use of non-thermal plasma for hydrocarbon reforming. *Chem. Eng. J.* **2005**, *106* (1), 59−71.

(20) Xi Zhen, L.; Liu, C. J.; Eliasson, B. Hydrogen production from methanol using corona discharges. *Chin. Chem. Lett.* **2003**, *14* (6), p631−633.

(21) Yan, Z.; Chen, L.; Wang, H. Hydrogen generation by glow discharge plasma electrolysis of ethanol solutions. *J. Phys. D: Appl. Phys.* **2008**, *41*, 155205.

(22) Babaritskii, A.; Baranov, I.; Bibikov, M.; Demkin, S.; Zhivotov, V.; Konovalov, G.; Lysov, G.; Moskovskii, A.; Rusanov, V.; Smirnov, R. Partial hydrocarbon oxidation processes induced by atmospheric-pressure microwave-discharge plasma. *High Energy Chem.* **2004**, *38* (6), 407−411.

(23) Ahn, J.; Holze, R. Bifunctional electrodes for an integrated water-electrolysis and hydrogen-oxygen fuel cell with a solid polymer electrolyte. *J. Appl. Electrochem.* **1992**, *22* (12), 1167−1174.

(24) Bockris, J. O. M.; Dandapani, B.; Cocke, D.; Ghoroghchian, J. On the splitting of water. *Int. J. Hydrogen Energy* **1985**, *10* (3), 179−201.

(25) Lozano-Parada, J. H.; Zimmerman, W. B. The role of kinetics in the design of plasma microreactors. *Chem. Eng. Sci.* **2010**, *65* (17), 4925−4930.

(26) Kim, D. B.; Rhee, J.; Moon, S.; Choe, W. Study of geometrical and operational parameters controlling the low frequency microjet atmospheric pressure plasma characteristics. *Appl. Phys. Lett.* **2006**, *89*, 061502.

(27) Fridman, A.; Chirokov, A.; Gutsol, A. Non-thermal atmospheric pressure discharges. *J. Phys. D: Appl. Phys* **2005**, *38*, R1−R24.

(28) Cochran, W. C.; Cox, G. M. *Experimental Design*; 2nd ed.; Wiley: New York, 1992.

(29) Abdul-Majeed, W. S.; Parada, J. H. L.; Zimmerman, W. B. Optimization of a miniaturized DBD plasma chip for mercury detection in water samples. *Anal. Bioanal. Chem.* **2011**, *401* (9), 2713−2722.

(30) Schutze, A.; Jeong, J. Y.; Babayan, S. E.; Park, J.; Selwyn, G. S.; Hicks, R. F. The atmospheric-pressure plasma jet: A review and comparison to other plasma sources. *IEEE Trans. Plasma Sci.* **1998**, *26* (6), 1685−1694.

(31) Sismanoglu, B.; Amorim, J. Microhollow cathode discharge and breakdown in micron separations. *Eur. Phys. J.—Appl. Phys.* **2008**, *41* (2), 165−172.

(32) Mollah, M.; Schennach, R.; Patscheider, J.; Promreuk, S.; Cocke, D. Plasma chemistry as a tool for green chemistry, environmental analysis, and waste management. *J. Hazardous Mater.* **2000**, *79* (3), 301−320.

(33) Akiyama, H. Streamer discharges in liquids and their applications. *IEEE Trans. Dielectrics Electrical Insulation* **2000**, *7* (5), 646−653.

(34) Hong, Y. C.; Uhm, H. S.; Yi, W. J. Atmospheric pressure nitrogen plasma jet: Observation of striated multilayer discharge patterns. *Appl. Phys. Lett.* **2008**, *93* (5), 051504−051504−3.

(35) Gordillo-Vázquez, F. J.; Camero, M.; Gomez-Aleixandre, C. Spectroscopic measurements of the electron temperature in low pressure radiofrequency $Ar/H_2/C_2H_2$ and $Ar/H_2/CH_4$ plasmas used for the synthesis of nanocarbon structures. *Plasma Sources Sci. Technol.* **2006**, *15*, 42.

(36) Nehra, V.; Kumar, A.; Dwivedi, H. Atmospheric non-thermal plasma sources. *Int. J. Eng.* **2008**, *2* (1), 53.

(37) Van der Sijde, B.; Van der Mullen, J. Temperature determination in non-LTE plasmas. *J. Quant. Spectrosc. Radiative Transfer* **1990**, *44* (1), 39−46.
(38) Lieberman, M. A.; Lichtenberg, A. J., *Principle of Plasma Discharge and Material Processing*, 2nd ed.; John Wiley & Sons, Inc.: New York, 2005.
(39) Bellan, P. M. *Fundamentals of Plasma Physics*; Cambridge University Press: Cambridge, 2006.
(40) Pacheco, M.; Pacheco, J.; Moreno, H.; Mercado, A.; Valdivia, R.; Santana, A. OES analysis in a nonthermal plasma used for toxic gas removal: Rotational and excitation temperature estimation. *Laser Phys.* **2008**, *18* (3), 303−307.
(41) Valdivia-Barrientos, R.; Pacheco-Sotelo, J.; Pacheco-Pacheco, M.; Mercado-Cabrera, A.; Jiménez-López, M. L.; Cruz-Azocar, V.; Ramos-Flores, F.; Durán-García, M.; Hidalgo-Pérez, a. M. Temperature evaluation of the nonthermal equilibrium of plasma discharges by OES analysis. *Laser Physics—Nonlinear Optics and Spectroscopy* **2008**, *18*, 298−302.
(42) Laux, C.; Spence, T.; Kruger, C.; Zare, R. Optical diagnostics of atmospheric pressure air plasmas. *Plasma Sources Sci. Technol.* **2003**, *12*, 125.
(43) Kado, S.; Sekine, Y.; Nozaki, T.; Okazaki, K. Diagnosis of atmospheric pressure low temperature plasma and application to high efficient methane conversion. *Catal. Today* **2004**, *89* (1−2), 47−55.
(44) Hill, S. J. *Inductively Coupled Plasma Spectrometry and Its Applications*; Wiley-Blackwell: Oxford, 2006; Vol. *7*.
(45) Laux, C. O. In *Radiation and Non-Equilibrium Collisional Radiative Models, in Physico-chemical Models for High Enthalpy and Plasma Flows*; Fletcher, D. G. et al., Eds.; VKI LS, Genese, Belgium (2002−2007), 2002.
(46) Stoffels, E.; Flikweert, A.; Stoffels, W.; Kroesen, G. Plasma needle: A non-destructive atmospheric plasma source for fine surface treatment of (bio) materials. *Plasma Sources Sci. Technol.* **2002**, *11* (4), 383.
(47) Masoud, N.; Martus, K.; Figus, M.; Becker, K. Rotational and vibrational temperature measurements in a high-pressure cylindrical dielectric barrier discharge (C-DBD). *Contrib. Plasma Phys.* **2005**, *45* (1), 32−39.
(48) Kitamura, N.; Sakamoto, T.; Matsuura, H.; Akatsuka, H. Dependence of vibrational and rotational temperatures of microwave discharge nitrogen−oxygen mixed discharge on their mixture ratio. *27th International Conference Phenomena in Ionized Gases, CD-ROM Proceedings*, 2005; pp 03−080.
(49) Eisenberg, G. Colorimetric determination of hydrogen peroxide. *Ind. Eng. Chem. Anal. Ed.* **1943**, *15* (5), 327−328.
(50) Kirkpatrick, M. J.; Locke, B. R. Hydrogen, oxygen, and hydrogen peroxide formation in aqueous phase pulsed corona electrical discharge. *Ind. Eng. Chem. Res.* **2005**, *44* (12), 4243−4248.
(51) Porter, D.; Poplin, M. D.; Holzer, F.; Finney, W. C.; Locke, B. R. Formation of hydrogen peroxide, hydrogen, and oxygen in gliding arc electrical discharge reactors with water spray. *IEEE Trans. Ind. Appl.* **2009**, *45* (2), 623−629.
(52) Team EPA. *A National Statistics Publication, Quarterly Energy Prices* ; Department of Energy and Climate: United Kingdom, 2012.
(53) Motret, O.; Hibert, C.; Pellerin, S.; Pouvesle, J. Rotational temperature measurements in atmospheric pulsed dielectric barrier discharge-gas temperature and molecular fraction effects. *J. Phys. D: Appl. Phys.* **2000**, *33*, 1493.
(54) Wei, D.; Lu, X.; Lu, Z.; Gu, J. Performance analysis and optimization of organic Rankine cycle (ORC) for waste heat recovery. *Energy Convers. Manage.* **2007**, *48* (4), 1113−1119.
(55) Zimmerman, W. B. Electrochemical microfluidics. *Chem. Eng. Sci.* **2011**, *66* (7), 1412−1425.
(56) Zhu, Z.; Zhang, S.; Lv, Y.; Zhang, X. Atomization of hydride with a low-temperature, atmospheric pressure dielectric barrier discharge and its application to arsenic speciation with atomic absorption spectrometry. *Anal. Chem.* **2006**, *78* (3), 865−872.
(57) Ross, D. Hydrogen storage: The major technological barrier to the development of hydrogen fuel cell cars. *Vacuum* **2006**, *80* (10), 1084−1089.
(58) Petitjean, L.; Ricard, A. Emission spectroscopy study of N_2−H_2 glow discharge for metal surface nitriding. *J. Phys. D: Appl. Phys.* **1984**, *17*, 919.
(59) Li, S. Z.; Huang, W. T.; Zhang, J.; Wang, D. Optical diagnosis of an argon/oxygen needle plasma generated at atmospheric pressure. *Appl. Phys. Lett.* **2009**, *94*, 111501.